Numerical modeling of electrowetting processes in digital microfluidic devices

Clime, Liviu; Brassard, Daniel; Veres, Teodor

Publisher's version / Version de l'éditeur:
https://doi.org/10.1016/j.compfluid.2010.05.003
Computers & Fluids, 39, 9, pp. 1510-1515, 2010-10-01

Computers & Fluids 39 (2010) 1510–1515

Contents lists available at ScienceDirect

Computers & Fluids

journal homepage: www.elsevier.com/locate/compfluid

Numerical modeling of electrowetting processes in digital microfluidic devices

Liviu Clime *, Daniel Brassard, Teodor Veres

National Research Council – Industrial Materials Institute, 75 Boulevard de Mortagne, Boucherville, Canada J4B 6Y4

ARTICLE INFO

Article history:
Received 28 October 2009
Received in revised form 5 May 2010
Accepted 6 May 2010
Available online 12 May 2010

Keywords:
Lattice Boltzmann
Electrowetting
Digital fluidics

ABSTRACT

We use a three-dimensional multiphase lattice-Boltzmann model to study basic operations such as transport, merging and splitting of nanoliter water droplets actuated by electrowetting in digital microfluidic devices. In a first step, numerical and analytical predictions for the droplet transport velocity are compared and very good agreement is obtained for a wide range of contact angles. The same algorithm is employed then to study the dynamics of the splitting processes at different contact angles and different geometries of the cell. The configuration of the liquid droplet involved in a splitting process and the dependence of the splitting time on the transport velocity are also investigated and phenomenological laws describing these processes are also proposed.

1. Introduction

Digital microfluidics [1] emerged as a second-generation architecture for lab-on-chip devices that is based upon the manipulation of discrete nanoliter volume droplets between two parallel plates (Hele-Shaw cells [2]). By applying a force locally on each individual droplet, digital microfluidic devices allow unit-sized packets of fluid to be transported, merged, mixed, split or stored in a discrete manner by using programmable external controllers [1]. Among the various mechanisms capable of manipulating discrete droplets on a surface (dielectrophoresis [3], thermocapillarity [4] and surface acoustic wave transport [5]), the electrowetting effect [6], defined as the change in the solid–liquid contact angle due to an electric potential difference between the solid and the liquid, offers the distinct advantage of being highly suitable for large scale integration on lab-on-chip devices. In such devices, the potential difference is applied between an array of individually controllable electrodes patterned on the bottom plate and a ground plane placed on the top plate. A microfluidic device consisting of a Hele-Shaw cell and an array of patterned electrodes on the bottom plate is usually referred to as an electrowetting-on-dielectric (EWOD) or digital microfluidic device.

In digital microfluidic devices, the droplets experience very complex geometrical changes, rapid displacements, and complicated internal recirculation of fluid when submitted to the electrowetting forces. To improve the reliability and accuracy of these devices, it is thus critically important to achieve a complete understanding of the fundamental processes involved in the manipulation of the droplets. Both analytical [7,2,8–10] and numerical [11–14] methods have been proposed in the past for this purpose. However, most of these studies have considered either (i) that the droplets are in static equilibrium [9,10,15,12], (ii) very simplified droplet geometries [15], or (iii) have involved some purely empirical parameters [8]. New methods are thus required before the complex processes occurring during the manipulation of the droplets can be fully understood.

The fundamental challenge in modeling such kind of processes consists mainly of the mesoscopic nature of the physical systems usually considered in digital microfluidics and nanofluidics. Classical approaches to computational fluidics based on discretizations of macroscopic continuum equations (like Navier–Stokes) present several difficulties [8,11] in dealing with wetting processes and contact line dynamics. On the other hand, molecular dynamics approaches, although successful for modeling wetting effects at the atomistic level (carbon nanotubes for example [16]), cannot be used for the sub-millimeter sized liquid droplets found in digital microfluidic devices as the number of atoms (molecules) is then simply too large for the actual computers. A relatively new numerical tool, designed to fill the gap between the microscopic (atomistic) level and the classical macroscopic methods is the lattice Boltzmann (*LB*) approach [17,18]. This new method, which is a numerical version of the continuous (full) Boltzmann equation, consists of simplified kinetic models incorporating the essential physics of microscopic or mesoscopic processes so that the macroscopic averaged properties obey the desired macroscopic equations [17]. The main strength of the *LB* method is that it behaves like a classical Navier–Stokes solver in the bulk liquid whereas its mesoscopic nature becomes important at the interfaces [19]. This advantage allows to easily address physical processes involving multicomponent or multiphase systems and complicated phenomena like contact line dynamics on complex boundaries.

* Corresponding author. Tel./fax: +1 450 641 5067.
E-mail address: Liviu.Clime@cnrc-nrc.gc.ca (L. Clime).

0045-7930/$ - see front matter Crown Copyright © 2010 Published by Elsevier Ltd. All rights reserved.
doi:10.1016/j.compfluid.2010.05.003

In this paper, we apply a 3D *LB* numerical algorithm in order to study basic operations in electroweting induced processes in digital microfluidic devices. The numerical results are compared to analytical models and simple phenomenological laws for the total splitting time of liquid droplets are given.

2. Numerical model

Several *LB* numerical schemes for addressing multiphase and multicomponent fluid flows are available in the literature. One of the first *LB*-based multicomponent model has been developed by Gunstensen and Rothman [20] and was based on the lattice gas model of Rothman and Keller [21]. Multiphase flows and phase separation have successfully been simulated by using the method of Shan and Chen [22,23], based on the use of an interaction pseudopotential between different phases (or components) of the system. Free-energy [24–26] and mean-field [27] *LB* approaches based on the themodynamics of two-component fluids and the free-energy thermodynamic functional can also be used for modeling multiphase and interfacial dynamics.

We numerically implemented a multiphase *LB* algorithm as described by Shan and Chen [22] and Shan and Doolen [23] by considering a three-dimensional lattice with 19 speeds (well known in the literature as the D3Q19 scheme [28]) denoted as $\vec{e}_i$, where i goes from 0 (particles at rest) to 18 (for the other predefined directions). The fluid particles at the nodes $\vec{x}$ of the lattice are interacting with their first-order neighbors (located at $\vec{x}+\vec{e}_i$) via an attractive short-range force of the form

$$\vec{F}(\vec{x}) = -G_{LL}\Psi(\vec{x})\sum_i w_i \Psi(\vec{x}+\vec{e}_i) \tag{1}$$

where G_{LL} is a negative quantity equivalent to the thermodynamic temperature and it is responsible for the liquid to vapor density ratio as well as the surface tension coefficient. Ψ is an interaction potential responsible for the equation of state (EOS) and equilibrium densities of the considered physical system (liquid and vapor) [29]. However, the choice of the interaction potential has to be made according to the relevant dimensionless number of the physical problem under investigation. In case of sub-millimeter sized droplets actuated by electrowetting, the surface tension and viscosity effects are dominant [30]. Thus, the capillary number

$$Ca = \frac{\eta U}{\gamma} \tag{2}$$

has to be considered. η and γ in the expression above are respectively the dynamic viscosity and the surface tension coefficient, whereas U is the droplet velocity. We have chosen an interaction potential that leads to one of the most stable EOS [31] that is

$$\Psi[\rho] = \Psi_0 \exp\left(-\frac{\rho_0}{\rho}\right) \tag{3}$$

where ρ stands for the fluid density whereas Ψ_0 and ρ_0 are constant parameters responsible for the equilibrium vapor and liquid densities. In our implementation, $G_{LL} = -120$, $\Psi_0 = 4$ and $\rho_0 = 200$ give a surface tension coefficient $\gamma^{LB} = 14.1$.

This value has been obtained by simulating liquid droplets of different radii and applying the Laplace law for the pressure difference across the free surface (Fig. 1a). The dynamic viscosities η^{LB} in the simulation are related to the collision time τ through the kinematic viscosity $v^{LB} = (\tau - 0.5)/3$ and the density ρ of the fluid (since $\eta^{LB} = v^{LB}/\rho$). In this paper, we consider the default value of the collision time $\tau = 1$ in the BGK collision term [32] therefore the two phases (equivalent liquid and gas) will present identical kinematic viscosities but different dynamic viscosities since different densities are obtained after the phase separation.

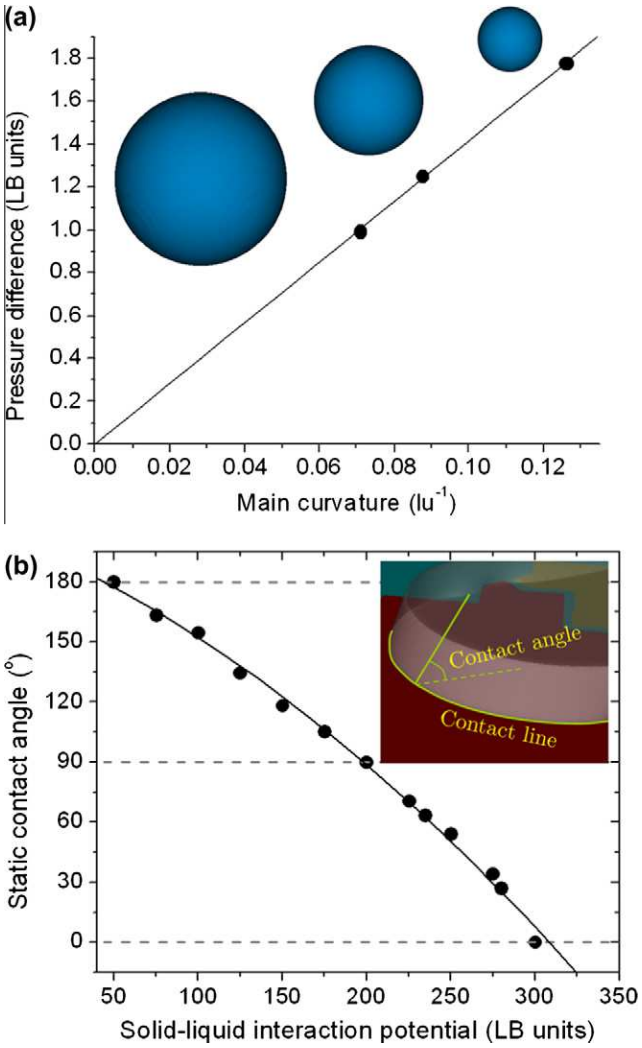

Fig. 1. (a) Linear fit with the Laplace's law of the pressure difference across spherical droplets of different radii; (b) simulated contact angles at the solid plates obtained by adjusting the interaction potential with the solid nodes.

The wettability of solid obstacles in the simulation (plates, electrodes and walls) is modeled by assuming a default value of the interaction potential Ψ (for example 1.0) at all the nodes inside these obstacles. Then the interaction constant G_{LL} in Eq. (1) is replaced with another constant G_{LS} (also negative) able to reproduce any desired contact angle of the liquid relative to the solid walls. As shown in Fig. 1b, a full range of contact angles from 0° to 180° can be obtained by appropriately tailoring the solid–liquid interaction potential. Note that the numerical values on the abscissa of this graph correspond to absolute (positive) values of the G_{LS} constant. It is worth mentioning that the quantity G_{LS} is not strictly related to the electrical voltage applied in a real electrowetting device. However, if necessary, such dependence can be obtained by correlating well known experimental electrical voltage dependencies of the liquid–solid contact angle to the numerical simulations presented in Fig. 1b. That is, the electrowetting equation as well as the problem of contact angle saturation in electrowetting [33] can be accounted for in a phenomenological manner. As for the actuation mechanism, by changing the contact angle at a certain region of the droplet, a change in the macroscopic curvature of the liquid free surface and consequently a difference in the internal pressure of the liquid droplet will be induced. Finally this difference in the internal pressure will eventually induce a displacement of the liquid against the

internal pressure gradient that is the droplet actuation. Further details on the difference between microscopic and macroscopic contact angles as well as a recent discussion on the different mechanisms of electrowetting actuation can be found in Ref. [34].

3. Parametrization of *LB* variables

The most important step in *LB* simulations is to relate abstract *LB* units of length and time (lu and ts, respectively) to real (physical) units (m and s). In this work, this is achieved by using the characteristic dimensionless number *Ca* as defined by Eq. (2). Since the capillary number *Ca* has to be identical in both lattice Boltzmann ("*LB*") and real ("*R*") physical systems, we impose

$$Ca = \frac{\eta^R U^R}{\gamma^R} = \frac{\eta^{LB} U^{LB}}{\gamma^{LB}} \tag{4}$$

By expressing the two velocities from the equation above and imposing the condition $U^R = U^{LB}$ we easily get

$$\left[\frac{\gamma^{LB}}{\eta^{LB}}\right]\frac{\text{lu}}{\text{ts}} = \left[\frac{\gamma^{R}}{\eta^{R}}\right]\frac{\text{m}}{\text{s}} \tag{5}$$

For water droplets we have $\gamma^R = 0.0725$ N m and $\eta^R = 0.001$ Pa s. Thus Eq. (5) reads now 1 lu/ts = 454 m/s. This value represents a relationship between the linear velocity in the *LB* space and the real world and can be used to relate *LB* units to physical length and time units. For example, if one lattice unit (lu) corresponds to 4.54 μm, a unit time (ts) accounts about 10 ns.

4. Numerical experiments

We consider a computational domain with $608 \times 262 \times N_z$ points in a regular lattice, where $N_z \in \{10, 16, 25\}$ are accounted for three different thicknesses H of the droplets (Fig. 2). All the nodes of this domain are considered as fluid nodes except those at the boundary that are set as solid nodes and both density and interaction potential initialized accordingly. Three squared comb-shaped electrodes [35] (denoted as A, B and C) with the size of about 110 lu are designed on the bottom plate (Fig. 2). If we consider 1 lu = 4.54 μm (as discussed in Section 3), this computational domain corresponds to a real EWOD system of 2.76 mm × 1.18 mm × H where H ∈ {45.4 μm, 72.54 μm, 113.5 μm}. Similarly, the size of the electrodes is of about 0.5 mm. The two extreme electrodes (A and C) are intentionally prolonged up to the boundary of the computational domain in order to facilitate the splitting. The interaction potential G_{LS} at these regions will be changed similarly with the actuation voltage in real EWOD devices. The equivalence between the constant G_{LS} and the electrical potential can be made through the contact angle at the solid–liquid–vapor separation (contact) line (inset of Fig. 1b). As for the top plate, it is considered homogeneous, that is the same interaction potential and density are set everywhere. A contact angle referred to as θ_{OFF} (corresponding to an interaction potential constant $G_{LS,OFF}$) is applied both on this top plate and to the regions outside the electrodes A, B and C on the bottom plate. The contact angle at activated electrodes can be changed by setting the interaction potential at these regions to a different value $G_{LS,ON}$ different from $G_{LS,OFF}$. The immediate effect of this change is that the contact angle at the activated electrodes will be changed with respect to the inactivated regions (plates). Consequently the curvature of the liquid free surface will be changed and a pressure difference (actuation) along the electrode chain will be generated. In this way, transport, splitting of merging of discrete droplets can easily be modeled by an appropriate time evolution of the interaction potentials at the active regions (nodes) of the plates. Thus, contrary to the previous approaches in modeling the transport of droplets in digital microfluidic devices, this model is very well suited to handle correctly the complex variations in the 3D geometry of the droplets with time. It can thus provide a more complete understanding on the transport velocity and dynamics of the operations performed on these devices.

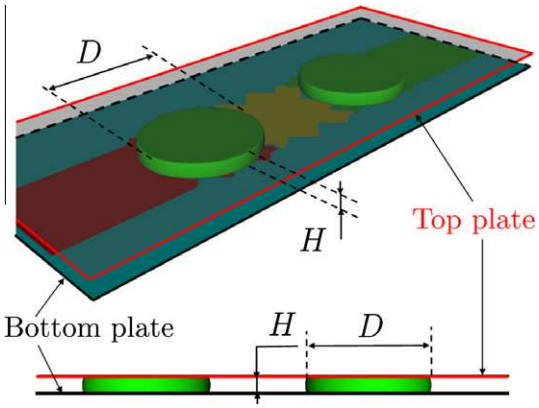

Fig. 2. Top and lateral view of the simulation scene considering two liquid droplets at equilibrium between the two parallel plates (Hele-Shaw cell). Three comb-shaped actuation electrodes are considered on the bottom plate.

5. Results and discussion

All the simulations start by considering two liquid droplets above the electrodes A and C and a timeline of the interaction potential with active and inactive regions as shown in Fig. 3a. Both inactive (plates) and active (electrodes) regions are initially set to a potential corresponding to θ_{OFF}. The size of the droplets at equilibrium is about the size of the electrodes $D \cong 0.5$ mm (Fig. 3b). At the time t_1 the electrode B is activated to an interaction potential G_{LS} corresponding to a contact angle $\theta_{ON} < \theta_{OFF}$. Consequently the two droplets will approach each other Fig. 3c) and merge in a single larger droplet. The electrode B is then turned off and the simulation continues up to the time t_2 until the equilibrium of the new formed droplet is attained (Fig. 3d). At the moment t_3 the electrodes A and C are activated to an interaction potential corresponding to $\theta_{ON} < \theta_{OFF}$ (Fig. 3e). The droplet elongates on the direction of the electrode chain and, if the electrowetting forces are strong enough, it splits into two smaller droplets located above the electrodes A and C (Fig. 3f). Then all the potentials on the electrodes are released to θ_{OFF} and two liquid droplets at equilibrium are obtained (Fig. 3g). Several simulations following the pattern sequence in Fig. 3a are performed at different *ON* and *OFF* contact angles and the transport velocity (before merging) as well as the splitting time of the liquid droplet computed. The main results of these simulations are comprised in Fig. 4a and b.

One of the main conclusions of the numerical analysis is that the transport velocity is directly proportional to the quantity $\Delta \cos\theta = \cos\theta_{ON} - \cos\theta_{OFF}$ (Fig. 4a). This is in rather good agreement with the analytical model [36] for the transport velocity U of a droplet of radius R and height H

$$U = \frac{\gamma H}{6\pi\eta R}\Delta\cos\theta \tag{6}$$

The expression above has been derived from the Navier–Stokes equations by neglecting inertia, the viscous drag due to surrounding gas as well as the contactangle hysteresis effects. In other words, the above simplified model results from the consideration of only two competing forces: the electrowetting actuation and the viscous friction (drag) between droplet and the metallic plates.

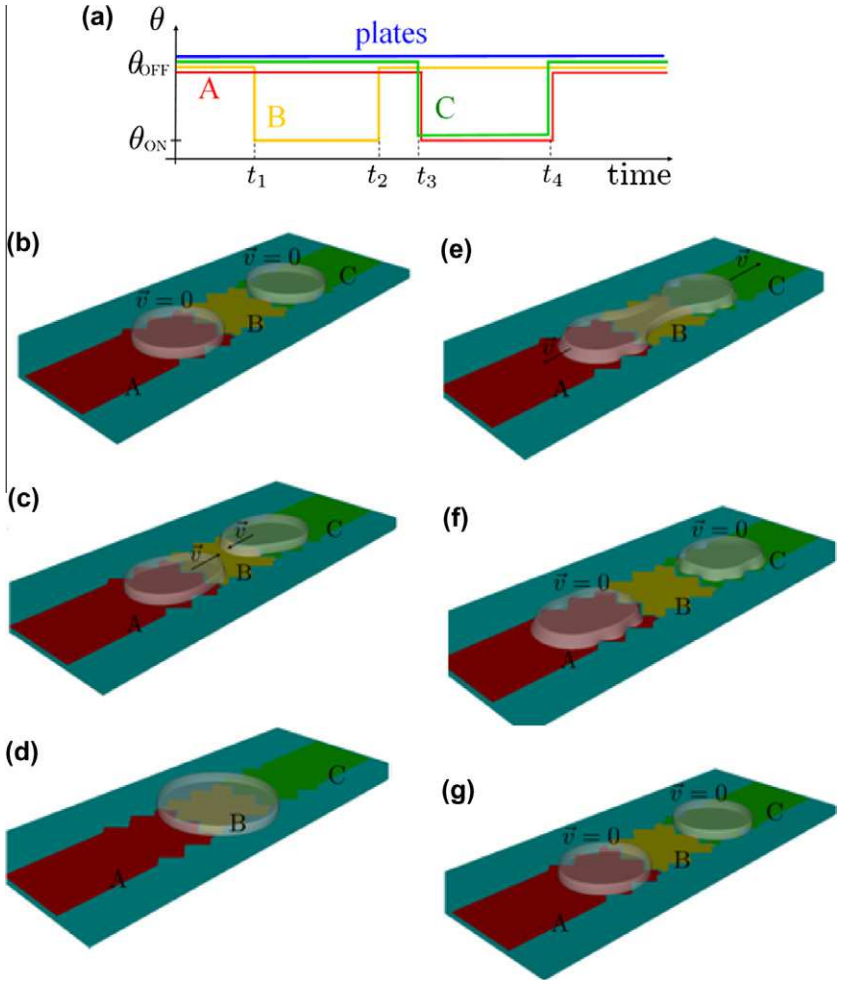

Fig. 3. (a) Time line of the interaction potentials corresponding to the simulation of a complex process on EWOD consisting of transport, merging and splitting liquid droplets; (b–g) different snapshots of the simulation from the initial configuration (b) until the splitting has been achieved (f).

As we shall see in the following, this simplified analytical model is reproduced relatively well by the numerical algorithm. The small difference between this analytical law and the numerical simulations can be explained by the deformation (elongation) of the droplet during the transport process. This deformation is equivalent to a decrease of the droplet hydrodynamic radius thus a slightly increase of the transport velocity at the same actuation pressure difference (solid and dashed lines in Fig. 4a). This indicates that, although simple analytical models can be used to predict reasonably well the transport of droplets in digital microfluidic devices, 3D *LB* simulations can provide a more complete and precise understanding of the phenomenon affecting the motion of the droplets.

After the equilibrium of the merged droplet is attained (time t_3), the splitting is started and the position of one leading edge of the droplet (inset of Fig. 3b) is recorded until the separation of the main droplet is achieved. The time evolution of this parameter follows a logarithm-like law and the critical positions corresponding to the actual break up of the droplet are almost identical (the ends of the splitting curves in Fig. 4b are characterized by approximately the same ordinate). Indeed, as shown in Fig. 5, the configuration of the droplet at the break up time does not change too much with the contact angles at active and inactive regions and seems to be dictated by the geometry of the electrodes only. The contact angles used in the simulations in Fig. 5 are indicated on each subfigure in the format θ_{ON}/θ_{OFF}. The slight change in Fig. 4e observed at very small *ON* contact angles $\theta_{ON} = 42^\circ$ is due to the fact that the droplet follows better the square shape of the electrodes such that the curvature of the free surfaces of the filament (link) before break up is slightly increased.

The splitting time, that is the difference between the time corresponding to the complete separation of the droplet and t_3 (i.e., the moment of activation of the electrodes A and C) is also evaluated at different values of the *ON* and *OFF* angles and different thicknesses *H* of the droplets (distance between the plates). A hyperbolic dependence of splitting time of the form

$$t(\Delta\cos\theta) = \frac{t_0}{\Delta\cos\theta - b} \tag{7}$$

is found to correspond to all investigated thicknesses (Fig. 6). A reasonable value of the parameter t_0 that fits all the points in Fig. 6 (solid lines) is about 0.3 ms. As for the parameter *b*, it is related to the critical value of $\Delta\cos\theta$ at which the splitting of the droplet becomes possible (note that for $\Delta\cos\theta = b$ we get $t \to \infty$). That is for a given spacing between the plates (droplet thickness) there are some critical combinations of *ON* and *OFF* contact angles (such that $\Delta\cos\theta > b$) which are capable of leading the droplet in a full break up process. The numerical values of the parameter *b* and the corresponding droplet thicknesses are given in Fig. 6.

Since the parameter *b* corresponds to the splitting threshold value for $\Delta\cos\theta$, it can be evaluated by analytical means also. A simple analytical expression for this critical value can be derived from the hydrostatic equilibrium of the droplet just before splitting [7]

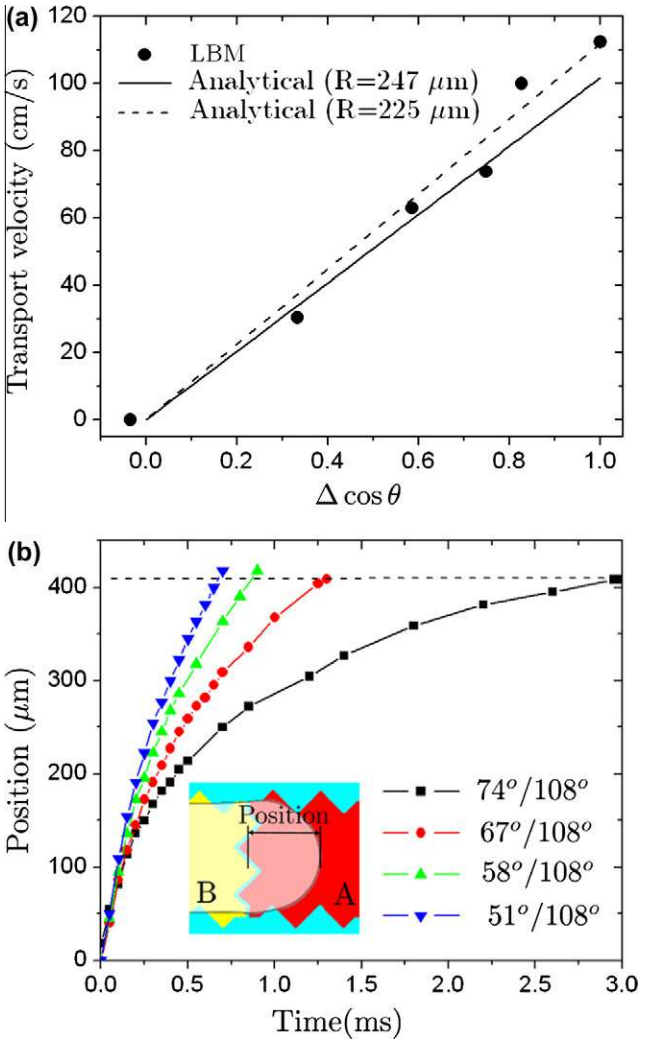

Fig. 4. (a) Numerical (points) and analytical (lines) modeling of the transport velocity in EWOD; (b) law of motion for the leading edge of a droplet involved in a separation (splitting) process.

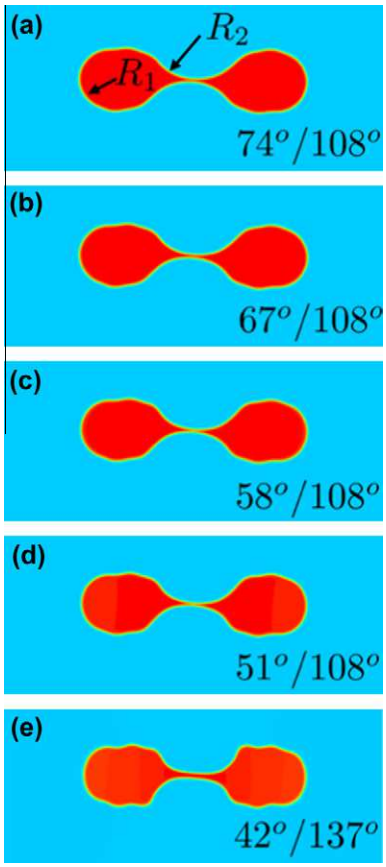

Fig. 5. Scalar cut planes in the density field of the simulation illustrating the geometrical configuration of the droplet just before the break up at different values of the *ON*/*OFF* contact angles. The slight corrugation of the droplet contour at small *ON* contact angles (more visible in d) originates in the tendency of the droplet to follow the shape of the electrodes.

$$\frac{R_1}{R_2} = 1 - \frac{R_1}{H} b \tag{8}$$

where R_1 and R_2 are the in-plane radii of curvature of the leading edge and necking region, respectively (Fig. 5a). R_2 is considered positive if the necking filament is convex and negative when it becomes concave. Obviously, in all situations depicted in Fig. 5, R_2 is negative since the droplet is almost at the splitting threshold and the in-plane profile of the liquid filament is concave. In a first approximation we can consider $R_1 = -R_2$ and the equation above becomes

$$b = \frac{2H}{R} \tag{9}$$

but for a better accuracy, both curvature radii of the droplet has to be considered, that is

$$b = H\left(\frac{1}{R_1} - \frac{1}{R_2}\right). \tag{10}$$

For the geometry considered here, the numerical values of the splitting thresholds for $H = 45.1$ μm, $H = 76.16$ μm and $H = 112.75$ μm are about 0.2, 0.3 and 0.5, respectively. Compared with the fit values from *LB* numerical simulations (legend of Fig. 6), an acceptable agreement is observed for the first two cases, especially

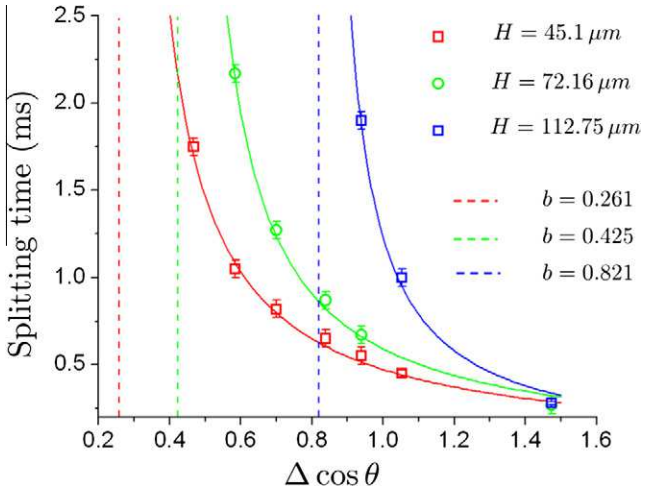

Fig. 6. Dependence of the splitting time on the quantity $\Delta \cos\theta$ for three different thicknesses of the droplet.

when the droplets are thinner. However, the two approaches become to disagree for thicker liquid droplets, the deviation being of about 37.5% from the *LB* numerical prediction in the case $H = 112.75$ μm. In our view, the observed discrepancies originate in the non-uniformities of the free surface curvature at the boundary of the electrodes and they become larger when distance between the plates gets larger. In other words, as the free surface

area of the liquid becomes larger, the variations of the contact angle along the contact line become smoother and the pressure differences responsible for the droplet splitting get smaller accordingly. This means that analytical thresholds like (8), (9) can be useful for splitting droplets of high aspect ratio (at least 10 for $2R/H$). At low aspect ratios (below 10), the free surface area to contour length ratio increases, and the above simple analytical model does not hold anymore. As such low aspect ratio are fairly common in digital microfluidic devices [6,7,30,35], our results highlight the importance of performing complete 3D dynamic analyses to predict reliably not only the kinetics but also the threshold conditions for the splitting of droplets.

6. Conclusions

The physical processes in EWOD devices can accurately be modeled by numerical lattice Boltzmann approaches. The basic processes involved in these devices are related to the viscosity of the liquid and the capillary forces at free liquid interface. Thus the capillary number *Ca* can be used as a characteristic dimensionless number for these phenomena. We found that the droplet transport velocities obtained from the lattice Boltzmann simulations are in good accord with the analytical Hele-Shaw model. However, some slight but significant differences were observed between the model and the *LB* simulations due to the deformation of the droplet that is not taken into account in the analytical model. The high versatility of the *LB* models also enabled us to measure the dynamics of operations involving much more complex geometries than simple droplet transport. For example, we found that the time required to perform the splitting of a droplet generally follows a hyperbolic law with an asymptotic behavior at the splitting threshold, where the required splitting time tends to infinity. Our results additionally indicate that the previous analytical models used to predict this splitting threshold would lead to significant inaccuracies for droplets with diameter to thickness aspect ratios larger than 10. This paper thus highlights the importance of using models, such as lattice Boltzmann, that are capable of performing dynamic analyses of complex 3D objects to fully grasp the phenomenon occurring during the manipulation of droplets in digital microfluidic devices.

Acknowledgement

Computational resources were provided by the Réseau québécois de calcul de haute performance (RQCHP).

References

[1] Pollack MG, Shenderov AD, Fair RB. Electrowetting-based actuation of droplets for integrated microfluidics. Lab Chip 2002;2:96.
[2] Hele-Shaw HS. The flow of water. Nature 1898;58:34.
[3] Gascoyne PRC, Vykoukal JV. Dielectrophoresis-based sample handling in general-purpose programmable diagnostic instruments. Proc IEEE 2004;92:22.
[4] Darhuber AA, Valentino JP, Trojan SM, Wagner S. Thermocapillary actuation of droplets on chemically patterned surfaces by programmable microheat arrays. J Microelectromech Syst 2003;12:873.
[5] Renaudin A, Tabourier P, Zhang V, Druhon C, Camart JC. Plateforme saw dédiée à la microfluidique discrète pour applications biologiques, 2ème Congrès Français de Microfluidique, Société Hydrotechnique de France; 2004. p. 14.
[6] Beni G, Hackwood S. Electro-wetting displays. Appl Phys Lett 1981;38:207.
[7] Cho SK, Moon H, Kim C-J. Creating, transporting, cutting, and merging liquid droplets by electrowetting-based actuation for digital microfluidic circuits. J Microelectromech Syst 2003;12(1):70.
[8] Sciffer S. A phenomenological model of dynamic contact angle. Chem Eng Sci 2000;55:5933.
[9] Almgren F. Minimal surface forms. Math Intel 1982;4(4):164.
[10] Almgren F, Taylor J. The geometry of soap films and soap bubbles. Sci Am 1976;7:82.
[11] Seppecher P. Moving contact angles in the Cahn–Hilliard theory. Int J Eng Sci 1996;34(9):977.
[12] Lienemann J, Greiner A, Korvnik JG. Modeling, simulation, and optimization of electrowetting. IEEE Trans CAD/ICAS 2006;25(2):234.
[13] Zeng J. Modeling and simulation of electrified droplets and its application to computer-aided design of digital microfluidics. IEEE Trans CAD/ICAS 2006;25(2):224.
[14] Zeng J, Korsmeyer FT. Principles of droplet electrohydrodynamics for lab-on-a-chip. Lab Chip 2004;4(4):265.
[15] Drygiannakis AI, Papathanasiou AG, Boudouvis AG. Manipulating equilibrium shape transitions of microdroplets in electrowetting – a computational analysis. Microelectron Eng 2009;86(4–6):1365.
[16] Schebarchov D, Hendy SC. Capillary absorbtion of metal nanodroplets by single-wall carbon nanotubes. Nano Lett 2008;8(8):2253.
[17] Chen S, Doolen GD. Lattice Boltzmann method for fluid flows. Annu Rev Fluid Mech 1998;30:329.
[18] Succi S, Benzi R, Higuera F. The lattice-Boltzmann equation – a new tool for computational fluid dynamics. Physica D 1991;47:219.
[19] Zhang J, Kwork DY. Lattice Boltzmann study on the contact angle and contact line dynamics of liquid–vapor interface. Langmuir 2004;20:8137.
[20] Gunstensen AK, Rothman DH. Lattice Boltzmann studies of immiscible two phase flow through porous media. J Geophys Res 1993;98:6431.
[21] Rothman DH, Keller JM. Immiscible cellular-automaton fluids. J Stat Phys 1988;52:1119.
[22] Shan X, Chen H. Lattice Boltzmann model for simulating flows with multiple phases and components. Phys Rev E 1993;47:1815.
[23] Shan X, Doolen GD. Multicomponent lattice-Boltzmann model with interparticle interaction. J Stat Phys 1995;81:379.
[24] Swift MR, Orlandini SE, Osborn WR, Yeomans JM. Lattice Boltzmann simulations of liquid–gas and binary-fluid systems. Phys Rev E 1996;54:5041.
[25] Swift MR, Osborn WR, Yeomans JM. Lattice Boltzmann simulation of nonideal fluids. Phys Rev Lett 1995;75:830.
[26] Aminfar H, Mohammadpourfard M. Lattice Boltzmann method for electrowetting modeling and simulation. Comput Methods Appl Mech Eng 2009;198(47–48):3852–68.
[27] Zhang J, Baoming L, Kwork DY. Mean-field free-energy approach to the lattice Boltzmann method for liquid–vapor and solid–fluid interfaces. Phys Rev E 2004;69:032602.
[28] Mei R, Shyy W, Yu D, Luo L-S. Lattice Boltzmann method for 3-d flows with curved boundaries. J Comput Phys 2000;161(2):680.
[29] Yuan P, Schaefer L. Equations of state in lattice Boltzmann model. Phys Fluids 2006;18:042101.
[30] Kumari N, Bahadur V, Garimella SV. Electrical actuation of dielectric droplets. J Micromech Microeng 2008;18:085018.
[31] Shan X, Chen H. Simulation of nonideal gases and liquid–gas phase transitions by the lattice Boltzmann equation. Phys Rev E 1994;49:2941.
[32] Bhatnagar PL, Gross EP, Krook M. A model for collision processes in gases. I: Small amplitude processes in charged and neutral one-component system. Phys Rev 1954;94:511.
[33] Mugele F, Baret J-C. Electrowetting: from basics to applications. J Phys: Condens Matter 2005;17:R705.
[34] Mugele F. Fundamental challenges in electrowetting: from equilibrium shapes to contact angle saturation and drop dynamics. Soft Matter 2009;5:3377.
[35] Brassard D, Malic L, Normandin F, Tabrizian M, Veres T. Water-coil core-shell droplets for electrowetting-based digital microfluidic devices. Lab Chip 2008;8:1342.
[36] Clime L, Brassard D, Veres T. Numerical modeling of electro-wetting transport processes for digital microfluidics. Microfluid Nanofluid 2010;8:599.